

Fusing data from the mesoscale model and radio remote sensing

L. T. Rogers and R. A. Paulus
NCCOSC RDTE DIV D883
49170 PROPAGATION PATH
SAN DIEGO CA 92152-7385

J. Cook
Naval Research Laboratory
Marine Meteorology Division
Monterey, CA 93943-5502

1 Introduction

The U.S. Navy has historically sponsored the development of mesoscale models and both in-situ and remote sensors. One of the driving forces behind these development efforts has been that the models and sensors can be used to estimate tropospheric refractivity gradients and therefore be used to provide input data to electromagnetic (EM) propagation models. The outputs of the EM propagation models are used as inputs to models designed to assess the performance (i.e. detection ranges) of radars and availability of communication systems.

To date, combining the outputs of the different sensors and the mesoscale model has been perceived as a computer and networking problem. While that work remains necessary, it must be realized that this is also an estimation problem. The ultimate goal of data fusion in refractivity estimation is the optimal estimation of propagation loss given information from the mesoscale model, radiosondes, refractivity inferred from radio measurements, in-situ, measurements at the sea surface, and from satellites and other remote sensors. This is a fundamentally different approach than that of traditional atmospheric data assimilation.

In this initial data fusion experiment we will focus on the mesoscale model and refractivity inferred from radio measurements. In many operational scenarios, the mesoscale model may be the only practical method for obtaining range dependent refractivity estimates. A weakness of the mesoscale model though, is that its inherent spatial averaging washes out sharp refractivity gradients at the capping inversion, which in turn results in underestimation of ducting effects. Radio measurements, on the other hand, are highly sensitive to the refractivity gradients in the capping inversion but remote sensing of refractivity by radio measurements is unlikely to ever provide range dependent refractivity when used by itself. VHF and UHF emitters are plentiful in many coastal areas and monitoring them for the purpose of inferring refractivity

is practical. Clearly, the two information sources are complementary and are excellent candidates for data fusion.

The data used are from the Variability of Coastal Atmospheric Refractivity (VOCAR) experiment (see *Paulus* [1994]) which took place June through September of 1993. The layout of the experiment is depicted in figure 1. Transmission links at 143, 262, and 374 MHz were operated on paths "A" and "B" that are shown in the figure. During a special two-week intensive observation period (IOP) beginning on August 23, 1993, radiosondes were launched at roughly four hour intervals from numerous locations including Point Mugu and San Clemente Island. Forecast refractivity fields were calculated from The Navy Operational Regional Atmospheric Prediction System (NO-RAPS) mesoscale model as described by *Hodur* [1987] and *Burk* and *Thompson* [1989]. Refractivity fields from the mesoscale model and the refractivity inferred from the transmission links are used to generate refractivity fields that preserve the range dependency of the mesoscale model fields, but also have a sufficiently strong trapping layer to be feasible given the measured propagation. The Research Vessel Point Sur was located at mid-path on Path A for roughly five days beginning August 27. The combination of the radiosondes from Point Mugu, San Clemente Island, and from the R.V. Point Sur are used to provide range-dependent profiles that provide validation for the data fusion method.

2 Objective of initial data fusion experiment

Figure 2 is an adaptation from *Kay* [1993] that illustrates the effect of the bias and variance of the estimator. The abscissa is estimation error and the ordinate is the probability. Ideally, we would like to have our estimation errors distributed as the minimum vari-

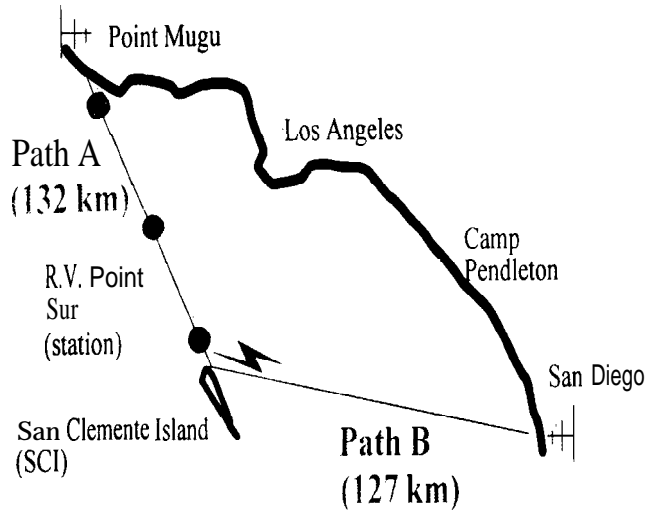


Figure 1: VOCAR layout.

ante unbiased estimator (MVUE) as shown in (a). In that case our estimation errors would be zero-mean and have the minimum variance achievable as determined by computation of the Cramer-Rao lower bound (CRLB) or other bounding criteria. If the errors have a variance greater than the lower bound but the estimates are unbiased, we might have (b). If the minimum variance is achieved but there is a non-zero bias we have (c), and if there is a non-zero bias and the minimum variance is not achieved we have (d).

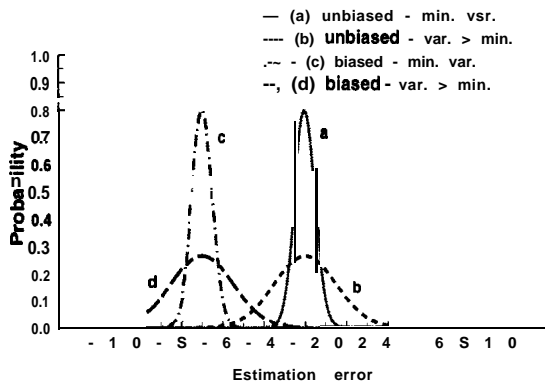


Figure 2: Illustration of variance and bias of estimation errors.

The situation using the mesoscale model by itself for propagation estimation is (d) since 1) the vertical resolution of the mesoscale model results in a non-zero bias, and 2) initialization and boundary condition errors result in greater than minimum variance. If the magnitude of the bias is nearly the same as, or greater than the square root of the variance, very little will be

achieved by reducing the error variance without reducing the bias. Accordingly, our goal in this effort is to utilize the radio measurements to unbiased the mesoscale model outputs while preserving the range dependent features of the mesoscale model.

3 VOCAR tri-linear model and parameterization

Figure 3 illustrates refractivity profiles corresponding to a standard atmosphere, a surface-based duct, and an elevated duct, and provides the geometry parameters used to describe the ducts. The surface-based-duct and elevated-duct profiles are associated with the marine boundary layer (MBL) capped by a stable layer. The stable MBL structure is quite common in areas such as the coastal waters of southern California and the Persian Gulf. The refractivity profiles associated with a stable MBL are often tri-linear in appearance.

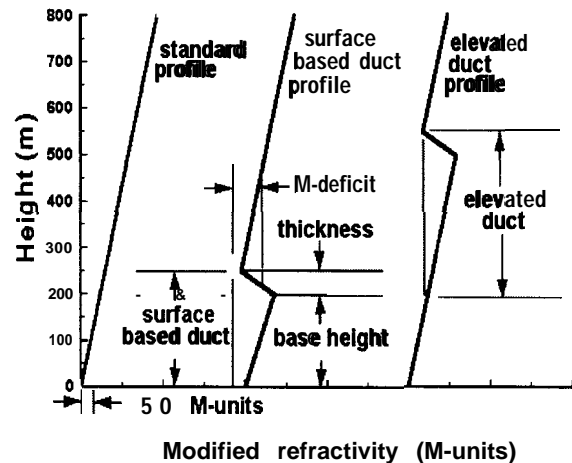


Figure 3: Idealization of refractivity profiles for duct -- formed by the capping inversion of the marine boundary layer.

In estimation problems it is customary to group parameters into deterministic parameters which we desire to estimate and nuisance parameters which we are not interested in, but must be accounted for, at least in the statistical sense [Kay, 1993]. The elements of

deterministic and random parameter vectors are of the form:

$$\Theta_D = [\theta_1, \theta_2, \dots, \theta_M]^T$$

and

$$\Theta_R = [\theta_{M+1}, \theta_{M+2}, \dots, \theta_N]^T$$

respectively. The utility of such a form is that nuisance parameters can be “integrated out”. Ideally, our nuisance parameters in this problem would characterize range and height variability in the refractivity structure that occur on time and spatial scales too small to predict, infer, or measure. In general, a function $g(\Theta_D, \Theta_R)$ is a point value corresponding to a single realization of Θ_R , while $y = g(\Theta_D)$ is a random variable. If $g(\cdot)$ is non-linear, then,

$$\overline{G(\Theta_D)} \neq G(\Theta_D, \overline{\Theta_R})$$

but

$$\overline{G(\Theta_D)} = \int_{\Theta_R} G(\Theta_D, \Theta_R) f_{\Theta_R}(\Theta_R) d\Theta_R$$

where $f_{\Theta_R}(\Theta_R)$ is the probability density function for the nuisance parameters. This is an important point in both the forward and inverse problem in tropospheric EM propagation: that you cannot determine mean propagation values (let alone distributions of propagation values) without accounting for the random processes of the propagation medium.

The deterministic parameterization implemented in this data fusion problem is:

$$\Theta_D = [h, m]^T \quad (1)$$

where h was the height of the base of the trapping layer in meters, and m was the M-deficit as shown in figure 3. The only random parameter was the thickness of the trapping layer d , i.e.

$$\Theta_R = \theta_3 = d \quad (2)$$

and d was assumed to be uniformly distributed over the interval 10 to 90 meters, i.e. the probability density function of θ_3 is

$$f_{\theta_3}(\theta_3) = \begin{cases} \frac{1}{90} & 10 < \theta_3 < 90 \\ 0 & \text{otherwise} \end{cases} \quad (3)$$

Clearly, this parameterization is far less sophisticated than an ideal parameterization which (as described before) would characterize the range and short term temporal variations in the refractive environment. Ideally,

its single random component approximates the effects introduced by the range and height variability in the true refractive environment. To some degree, this is the case; using a waveguide-mode model, it can be observed that when d is varied it tends to make large changes in the relative phase and amplitudes of the dominant propagation modes which lead to constructive and destructive interference effects that resemble those introduced by the true (dominantly range) variability. Nonetheless, as described in *Rogers [1996]*, the parameterization works poorly with weak trapping layers and should be the primary area of focus in future work.

4 Input data

4.1 NORAPS mesoscale model runs for the VOCAR experiment

The mesoscale weather prediction model used to simulate the 12 day VOCAR IOP is a version of the Navy Operational Regional Atmospheric Prediction System (NORAPS) described by *Hodur [1987]* and *Burk and Thompson [1989]*. NORAPS is a hydrostatic primitive equation model with sophisticated second-order closure boundary layer physics which are important for describing near-surface atmospheric (and refractive) structures. The domain for the VOCAR experiment extends from Oregon to Baja California and from Arizona to about 1000 km off the California coast. The horizontal resolution is 20 km and the terrain following, 30 level, vertical coordinate system is distributed so that the resolution is greatest near the surface of the earth and decreases upwards. This scheme allows us to resolve the large vertical gradients in temperature and moisture typically found near the surface that are critical for evaluating refractive effects. NORAPS was run twice daily in a data assimilation mode to provide 24 h forecasts, with data archived every four hours during the forecast periods. Data assimilation is important because there is not enough data to adequately define the structure of the atmosphere across the model's domain. In the data assimilation method, the previous 12 h forecast is used as a starting point and observed data is incorporated with an optimum interpolation analysis in order to initialize the next forecast. In this way, details of atmospheric structures are maintained from one model forecast to the next and are modified using available data. This process is repeated every 12 h to maintain an updated forecast based on the most current condi-

tions. Over water, the sea surface temperature field is updated every 24 h and fixed during the intermediate forecast periods.

4.1.1 Meteorological evaluation of NORAPS VOCAR performance

The performance of NORAPS during VOCAR has been documented in *Burk et al., [1994]* and *Burk and Thompson [1994]*. NORAPS forecast a typical California coastal summertime pattern during the beginning of the VOCAR experimental period. The predominate northerly flow aloft along the central California coast topographically forced a large-scale eddy in the bight which resulted in weak southerly flow immediately adjacent to the coast. This weak pattern allowed a significant diurnal variation in the atmospheric boundary layer and associated elevated trapping layer to develop. The trapping layer tended to be low at midday and then elevate and weaken at night. The diurnal variability decreased sharply westward, away from the coastline; at the location of the R/V POINT SUR, the diurnal behavior was discernible but not nearly as pronounced as at Pt. Mugu. As the experiment progressed, the northerlies turned more northeasterly and an eddy developed off the northern California coast, in the lee of the Siskiyou and Klamath mountain ranges. The eddy developed into a mesoscale low that drifted southward and caused the winds in the bight to shift to the west. This movement of the low caused the boundary layer in the bight to deepen and the trapping layer and associated duct to rise and weaken. The boundary layer adjacent to the coast just north of Point Conception was forecast to be somewhat shallower due to divergence associated with the acceleration of a lowlevel jet just above the boundary layer. During this period, NORAPS forecast a weakening of upper level subsidence and the advection of moist air aloft. These two features resulted in the trapping layer rising and weakening over time. Comparison with individual soundings show that NORAPS correctly forecast the atmospheric boundary layer and trapping layer trends during the early and middle VOCAR periods, although the depth of the boundary layer (height of the trapping layer) was under forecast. The causes of these forecast errors have been attributed to the initialization procedure and to over-forecasts of near surface heating caused by the crude representation of the offshore islands [*Burk and Thompson, 1994*].

4.2 Refractivity inferred from propagation measurements

The inference of refractivity parameters from the VOCAR EMpropagation data is discussed in *Rogers, [1996]*; only a brief outline will be given here. As described in section 3, $\Theta = [\Theta_D; \Theta_R]^T = [h, m; d]^T$ is a parameter vector describing a single realization of the refractive environment. $g(\Theta, f)$ is the propagation factor at frequency f associated with refractivity realization Θ . The mean propagation factor over the realizations of Θ_R is $\overline{g(\Theta_D, f)}$. In vector form, we have

$$\overline{G(\Theta_D)} = \begin{bmatrix} \overline{g(\Theta_D, f_1)} \\ \overline{g(\Theta_D, f_2)} \\ \overline{g(\Theta_D, f_3)} \end{bmatrix}$$

where $\overline{G(\Theta_D)}$ is the column vector of mean propagation factors associated with deterministic parameter vector Θ_D over the various realizations of random parameter vector Θ_R . At a single frequency f , $\overline{g(h, m, f)}$ can be pictured as contour plot in the h, m parameter space. This is illustrated in figure 4 which illustrates contours of constant propagation factor for the geometry and frequencies of the VOCAR experiment.

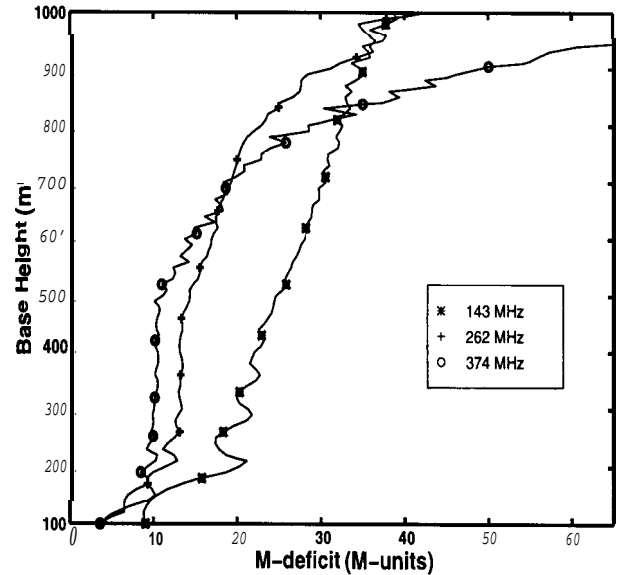


Figure 4: Three contours, each corresponding to a constant propagation factor of $F = -30$, for the three VOCAR frequencies.

$Y(t) = [y_1(t), y_2(t), y_3(t)]^T$ is the vector of measured propagation factor at the three VOCAR fre-

quencies at time t . The summed squared error of estimating the propagation factor at time t using propagation factors corresponding to Θ_D is

$$R(t, \Theta'_D) = (Y(t) - \overline{G(\Theta_D)})^T (Y(t) - \overline{G(\Theta_D)}), \quad (4)$$

where T is used to indicate the transpose.

Determining an effective error variance term σ_{eff}^2 (to account for modeling and measurement errors) by a *a posteriori* maximum likelihood computation, $f_{Y(t)|\Theta_D}(Y(t))$ (the probability density of observing propagation factors vector $Y(t)$, given that the environment vector Θ_D is equal to Θ'_D) is

$$f_{Y(t)|\Theta_D}(Y(t) | \Theta'_D) = \frac{e^{-\frac{1}{2\sigma_{eff}^2} R(t, \Theta'_D)}}{(2\pi)^{3/2} \sigma_{eff}}.$$

The form of 5 is the result of assuming that the three individual elements of $Y(t) - \overline{G(\Theta_D)}$ have independent identically distributed Gaussian distributions.

Applying Bayes' rule we have

$$\Pr(\Theta'_D | Y) = \frac{f_{Y(t)|\Theta_D}(Y(t) | \Theta'_D) f_{\Theta_D}(\Theta'_D)}{\int_{-\infty}^{\infty} f_{Y(t)|\Theta_D}(Y(t) | \Theta_D) f_{\Theta_D}(\Theta_D) d\Theta_D},$$

where $f_{\Theta_D}(\Theta_D)$ is our prior density of Θ_D and the prime (') is used to indicate that Θ'_D is a single combination of the h and m . In this problem, it was assumed that elements of Θ_D were uniformly distributed over the parameters space W defined by

$$\Theta_D \subset W \rightarrow \begin{cases} 200 < h < 1000 \\ 0 < m < 65 \end{cases} \quad (5)$$

where the limits of the parameters space were based upon examination of the VOCAR radiosondes. Consequently, the previous equation can be reduced to

$$\Pr(\Theta'_D | Y) = \frac{f_{Y(t)|\Theta_D}(Y(t) | \Theta'_D)}{\int_W f_{Y(t)|\Theta_D}(Y(t) | \Theta_D) d\Theta_D}.$$

It should be noted that while (in this case) the prior information has been used only to limit the parameter space to feasible values, the prior distribution is the way by which climatology can be incorporated into the estimation algorithm.

An example of inferring parameter values from measured propagation is shown in figure 5. We assume that at time t , a measured propagation factor vector of $Y = [-30 \ -30 \ -30]^T$ is recorded. The relative likelihood of any particular combination of h and m is proportional to the shading where lighter shading indicates higher likelihood.

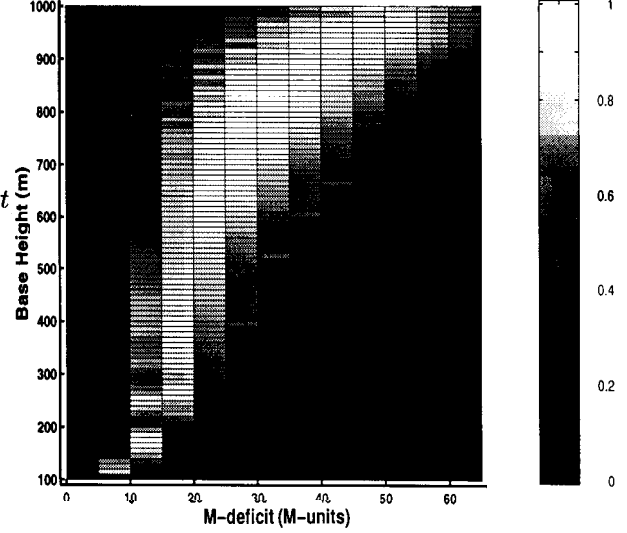


Figure 5: Relative likelihood of height h and M-deficit m corresponding to measured propagation factors vector of $Y(t) = [-30 \ -30 \ -30]^T$ for the VOCAR frequencies and geometries.

As with the parameterization discussed in section 3, there are weaknesses with this procedure. The greatest of these is the assumption that the mismatches (i.e. the values of $Y(t) - \overline{G(\Theta_D)}$) are Gaussian processes and are invariant over the parameter space.

5 Validation data

To prepare height-range cross sections of refractivity for the Radio Physical Optics (RPO) program, the refractivity structure matching algorithm (RSMA) was developed by Vogel [1991] and modified by Cook *et al.*, [1994]. Processing by RSMA guarantees that two important input data requirements for RPO are met: a) every profile contains the same number of levels, and b) the n th level in any one profile is matched to a refractivity structure at the n th level in all the other profiles. The matching of common refractive layers is accomplished in three steps. First, each level in every profile is categorized based on its refractivity structure type. The top and bottom levels are all assigned to the same category to ensure they are always matched up. Second, the primary structure types considered important for propagation are matched between adjacent profiles within physically reasonable bounds.

The matching is done iteratively, so that like structures near the same altitude are matched first. This procedure ensures the layers transition smoothly in refractive effect and altitude. Many refractive structures/pairings are considered minor and are ignored by RSMA. Third, all the remaining profile levels are matched using a secondary “best fit” algorithm that connects all the unmatched points between the primary matched levels. Any remaining unmatched points are interpolated in between the matched levels to force the structures to be consistent from profile to profile.

For this study, 14 marine cross sections were identified during VOCAR where the data were collected within about one hour of each other. Each cross section consists of three profiles starting at San Clemente Is. (NUC), runs through the NPS R/V Point Sur near the center (SUR), and ends at Pt. Mugu (NTD). Table 1 lists the profiles and the mean starting times which were used for comparison with the four hourly NORAPS data. Because RSMA was not designed to process the large number of vertical levels and fine structure associated with the profile measurements, a simple preprocessing step was required to reduce the data and make further processing feasible. The reduction was accomplished by fitting straight line segments to the profiles while preserving the important refractive structures determined by a criterion that depends on height. The criterion used was a 1/4 m-unit root-mean-square (RMS) deviation at the surface which increased three m-units per kilometer altitude. This line-fitting procedure preserved structures near the surface and considerably simplified the profiles aloft. The resulting profiles were then processed by RSMA and formatted for input into RPO. In general, the cross sections depict initially a stratified atmosphere with a strong surface-based duct, due to an elevated trapping layer whose height tends to be lowest at mid path (R/V POINT SUR). With time, the boundary layer shallows slightly then, early on 28 Aug., the boundary layer rapidly deepens, raising the elevated trapping layer and the duct. The later cross sections also describe a more homogeneous atmospheric condition, both as a function of range with a consistent trapping layer height, and as a function of height with the atmosphere exhibiting much less stratification.

6 Performance

Before examining overall results, two “events” are examined: serial days 239.167 and 241.666. The former is an instance where using the mesoscale model

Table I: VOCAR cross sections from San Clemente Island (NUC), through the R/V POINT SUR (SUR), and to Pt. Mugu (NTD). Times are Pacific Standard Time (PST).

#	Calendar date	Serial day
1	25 Aug. 1933	237.833
2	26 Aug. 1556	238.666
3	27 Aug. 0346	239.167
4	27 Aug. 0735	239.333
5	27 Aug. 1532	239.666
6	28 Aug. 0338	240.166
7	28 Aug. 0741	240.333
8	28 Aug. 1555	240.666
9	28 Aug. 1934	240.833
10	29 Aug. 0341	241.167
11	29 Aug. 0743	241.333
12	29 Aug. 1528	241.666
13	29 Aug. 1928	241.833
14	30 Aug. 0341	242.133

generated refractivity profiles results in a significant negative bias in resulting propagation estimates. Consequently, the additional information from the inverse medium problem significantly improves the accuracy of propagation estimates. In the latter case, the mesoscale model refractivity estimates have high fidelity to the true environment so that the addition of information from the inverse medium problem does not significantly improve propagation estimation.

6.1 Date serial 239.167

The upper plot in figure 6 is a cross section of the refractivity fields constructed from the NORAPS temperature and humidity fields as described in section 4.1. The lower plot in figure 6 is vertical refractivity profiles for the same cross section that have been joined using the RSMA algorithm as described in section 5. Comparing the two graphs, the following is noted:

- 1 The average height of the base of the trapping layer is roughly the same in both the NORAPS generated profiles and the RSMA-processed measured profiles,
- 2 The same downward-sloping base of the trapping layer is observed in both sets of profiles.

3. The strength of the trapping layers is much, much stronger in the RSMA-processed measured profiles.
4. In the measured profiles, a weakening of the trapping layer with respect to range is observed. In the mesoscale profiles, the same, albeit weaker trend is observed.

These two plots considered thus far illustrate just how well the mesoscale model forecast can capture the horizontal evolution of the refractivity structure. They also illustrate how much weaker the trapping layer representations from the mesoscale model can be with respect to the measured values.

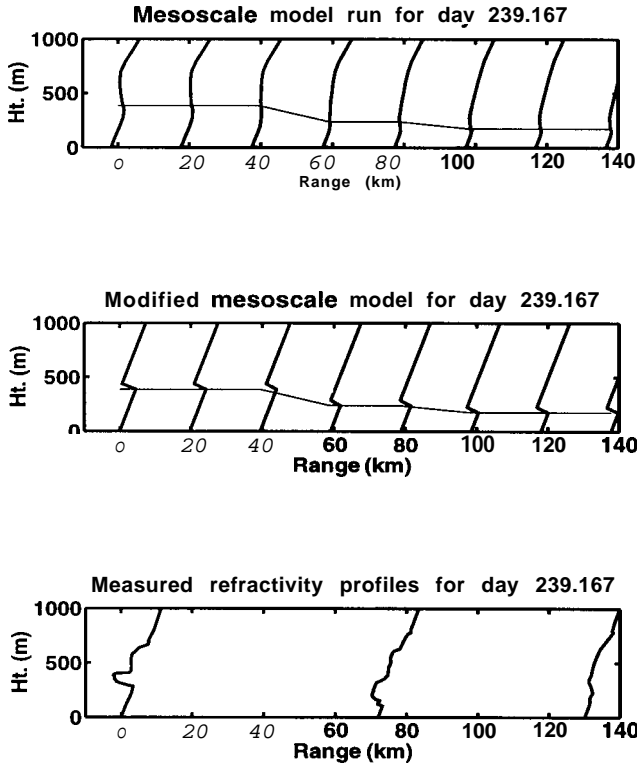


Figure 6: Refractivity cross sections for serial day 239.167 from the mesoscale model, modified (or data-fused) profiles, and from measured profiles respectively. The thin line in each the the first two plots indicates the height of the base of the trapping layer h .

6.1.1 Application of bias correction

The application of the bias-correction method is illustrated in figure 7. Obtaining the conditional probab-

ity distribution $\Pr(\Theta_D|Y) = \Pr(h, m|Y)$ is described in section 4.2. A line of feasible solutions in the $\{h, m\}$ parameters space is calculated from $\Pr(h, m|Y)$ using

$$\{h, m\}_{FEAS} = \text{Max}_m(\Pr(h, m|Y)).$$

This is equivalent to saying that once we have observed Y , that for given height h , the feasible value of m is the one that maximizes $\Pr(h, m|Y)$.

Next, the averages \bar{h}_{MES} and \bar{m}_{MES} , are computed from $h_{MES}(r)$ and $m_{MES}(r)$, the range (?) dependent values of base height and M-deficit calculated from the NORAPS generated refractivity fields (hence the subscript *MES*). The local gradient

$$\left\{ \frac{\partial L}{\partial h}, \frac{\partial L}{\partial m} \right\}_{h_{MES}, m_{MES}},$$

is computed numerically. Moving in the direction of that local gradient we intersect the line of feasible solutions. That is our value of $(\bar{h}_{MOD}, \bar{m}_{MOD})$ where the subscript *MOD* is used to denote that these are the modified (or data fused) parameter values. Now a set of tri-linear profiles are determined such that:

$$h_{MOD}(r) = \bar{h}_{MOD} + h_{MES}(r) - \bar{h}_{MES} \quad (6)$$

$$m_{MOD}(r) = \bar{m}_{MOD} + m_{MES}(r) - \bar{m}_{MES}. \quad (7)$$

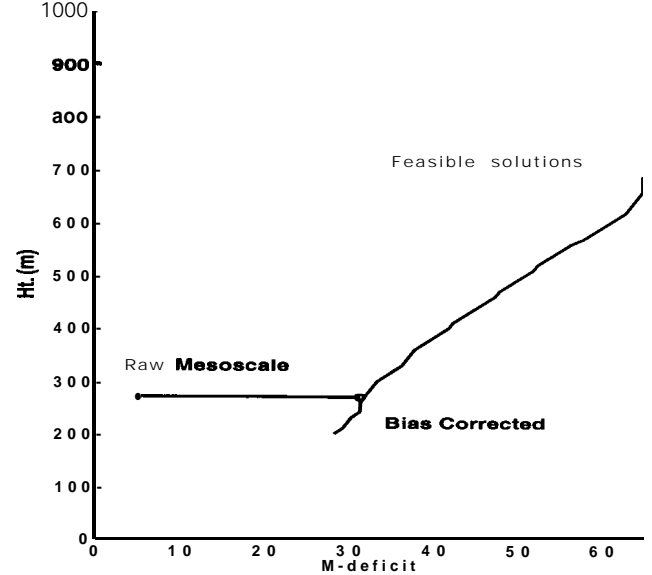


Figure 7: Parameter space for serial day 239.167.

The data-fused tri-linear profiles appear in the middle plot in figure 6. It is clear that the trapping layer strengths are substantially greater than those

observed in the raw mesoscale model outputs. Additionally, the range dependency of the base heights has been preserved and closely matches that of the measured profiles. There is a minor weakening in the trapping layer with respect to range in the modified profiles, but it is less pronounced than in the measured profiles.

6.2 Date serial 241.666

While on date serial 239.167, there exists a large difference between the mesoscale model predicted and the measured refractivity profiles, on date serial 241.666, the predicted and measured were quite close as can be seen in figure 8. As a consequence, the bias correction is small and the bias corrected profiles do not differ significantly from either the predicted or measured profiles.

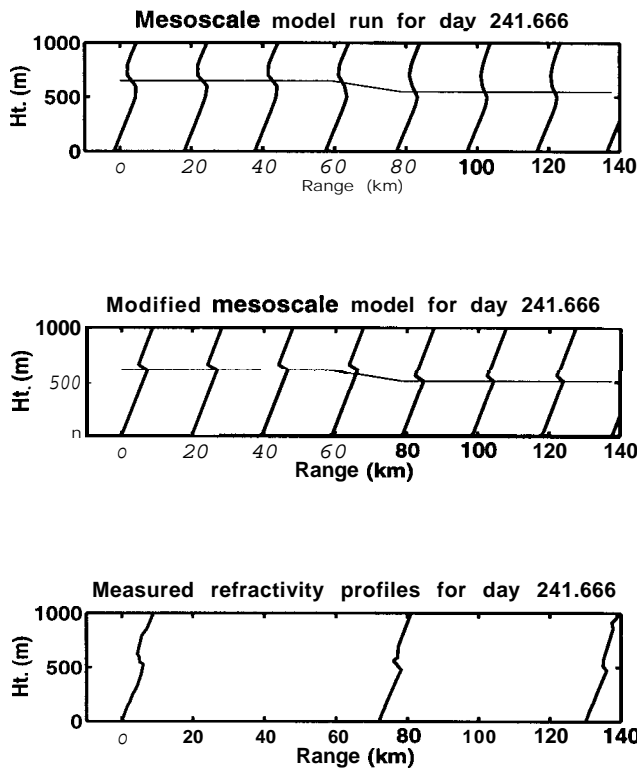


Figure 8: Refractivity cross sections for serial day 241.666.

6.3 Overall results

Figure 9 is a time series of propagation factors at 1000 GHz predicted using (a) radiosonde profiles pro-

cessed using RSMA as described in section 5, (b) mesoscale model generated refractivity fields as described in section 4.1, and (c) bias corrected tri-linear profiles generated as described in section 6.1.1. It is clear that the while there are times where using the raw mesoscale model fields results in accurate refractivity estimates, there are times when their use does not. In those cases (i.e. the first three data points), the bias corrected profiles provide much better estimates.

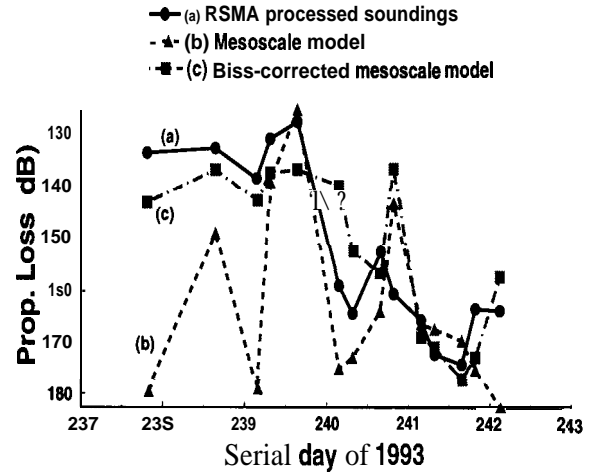


Figure 9: Time series of propagation factors at 1.0 GHz.

7 Summary

A simple algorithm has been implemented to fuse data from the mesoscale model with parameter values inferred from radio remote sensing. The major points from the work include:

1. Weaknesses:

- (a) The parametrization used is heuristic in nature and based largely upon observations of the behavior of the capping inversion layer in the Southern California bight.

- (b) With results based upon only five days of test data from only a single geographical region, the representativeness of the results is open to question.
- (c) There is no "physics" in the parameter space movement.

2. Strengths:

- (a) As is illustrated in figure 9, the intended objective, unbiassing the mesoscale model, is achieved.
- (b) The implementation is computationally simple.

7.1 Future direction

What direction the data fusion efforts should take is a function of Navy needs. In this paper we have used measured propagation data to improve mesoscale model refractivity fields. An equally pressing need is to be able to incorporate local radiosonde data into mesoscale model fields. The key element in both of these problems is parameterization.

Ultimately, a parameterization will be developed combining two very different techniques. First, large-eddy-simulation (LES) such as described in *Otte, et al. [1996]*, and *Khanna, et al. [1996]* are used to develop parameterizations and other techniques that makes sense meteorologically. Equally important is to perform the sensitivity analysis to determine the modeling/parameterization that is optimal from a propagation estimation standpoint.

Acknowledgments

Radiosondes from San Clemente Island and Point Mugu courtesy of the Naval Air Warfare Center, Point Mugu, California. The mid-path radiosondes were launched from the Research Vessel Point Sur which was operated by the Naval Postgraduate School, Monterey, California. This work was funded by the Office of Naval Research.

References

- [1] Burk, S.D., W.T. Thompson, J. Cook, and G.G. Love, "Mesoscale modeling of refractive conditions during the VOCAR experiment," *Proc. IGARSS*, Pasadena, CA, 1994.
- [2] Burk, S.D. and W.T. Thompson, "Mesoscale modeling of refractive conditions in a complex coastal environment," *AGARD CP 567*, pp 40.1-40.7, 1994.
- [3] Burk, S.D. and W.T. Thompson, "A vertically-nested regional numerical weather prediction model with second order closure physics," *Mon. Wea. Rev.*, 117, pp 2305-2324, 1989.
- [4] Cook, J., G. Vogel and G. Love, "Operational support for a range-dependent radio propagation model," *AGARD CP 567*, pp 13.1-13.8, 1994.
- [5] Kay, S.M. "Fundamentals of statistical signal processing. estimation theory," Prentice Hall PTR, Upper Saddle River, NJ 07458, 1993
- [6] Khanna, S., J.G. Brasseur, J.C. Wyngaard, "The local structure of the atmospheric boundary layer," *Proc. Battlespace Atmosph. Conf.*, 3-5 Dec. 1996, NRD TD 2938, 1996
- [7] Hodur, R. M., "Evaluation of a regional model with an update cycle," *Mon. Wea. Rev.*, 115, pp. 2707-2718, 1987,
- [8] Otte, M. J., N.L. Seaman, D.R. Stauffer and J.C. Wyngaard, "A mesoscale model for EM ducting in the marine boundary layer," *Proc. Battlespace Atmosph. Conf.*, 3-5 Dec. 1996, NRD TD 2938, 1996
- [9] Paulus, R. A., "VOCAR: An experiment in the variability of coastal atmospheric refractivity," *Proc. IGARSS*, Pasadena, CA, 1994.
- [10] Rogers, L. T., "Likelihood estimation of tropospheric duct parameters from horizontal propagation measurements," accepted by *Radio Science*, Sep., 1996
- [11] Vogel, G. N., "Specification for a refractivity structure matching algorithm," NOARL Tech. Note 191, Naval Research Lab., 1991.